PCCP

PAPER

View Article Online
View Journal | View Issue

Cite this: *Phys. Chem. Chem. Phys.*, 2016, **18**, 2070

In situ study of copper reduction in $SrTi_{1-x}Cu_xO_3$ nanoparticles†

Vitor C. Coletta,[a] Francielle C. F. Marcos,[b] Francisco G. E. Nogueira,[b] Maria I. B. Bernardi,[a] Alain Michalowicz,[c] Renato V. Gonçalves,[a] Elisabete M. Assaf[b] and Valmor R. Mastelaro*[a]

Received 3rd October 2015,
Accepted 2nd December 2015

DOI: 10.1039/c5cp05939a

www.rsc.org/pccp

Perovskite strontium titanate is a promising functional material for gas sensors and catalysis applications. Herein, we report the preparation of $SrTi_{1-x}Cu_xO_3$ nanoparticles with Cu doped in the B sites using a modified polymeric precursor method. This study describes in detail the structural and local atomic configurations for the substitution of Cu into the titanium sites and its reducibility using X-ray diffraction (XRD), field emission gun scanning and transmission electron microscopies (FEG-SEM and TEM), X-ray absorption spectroscopy (XAS), X-ray photoelectron spectroscopy (XPS) and temperature-programmed reduction (TPR) analyses. Our results indicate that copper is segregated for $x \geq 0.06$. After exposing the samples to a hydrogen-rich atmosphere at temperatures over 500 K, copper is reduced from Cu^{2+} to metallic Cu. This reduction was attributed to copper atoms that originated primarily from the CuO phase.

Introduction

Strontium titanate ($SrTiO_3$) is a perovskite oxide that has been investigated for use in a wide range of applications such as gas sensors,[1–3] fuel cell electrodes,[4] luminescence,[5–7] catalysis[8–13] and photocatalysis.[14–16] The partial substitution of Sr and/or Ti ions in the lattice can modify some of the properties of $SrTiO_3$, making it more attractive for desired applications. For example, the occupation of titanium sites by another transition metals with a different valence can create oxygen vacancies to maintain charge neutrality.[3] $SrTi_{1-x}Fe_xO_3$ has been studied for use in ozone[1] and oxygen gas sensors.[2] The substitution of Ti by Mn ions to form the $SrTi_{1-x}Mn_xO_3$ system led to a decrease in the bandgap relative to that of pure $SrTiO_3$, making the $SrTi_{1-x}Mn_xO_3$ system suitable for photocatalysis applications.[16]

Recently, $SrTiO_3$ has been studied for catalysis applications, both as a support for metallic nanoparticles[8,9] and by a substitution of Ti ions,[10–13] due to its stability at high temperatures[9,11] and the possibility of keeping the incorporated ions dispersed in the latter case.[11] Glisenti *et al.* obtained a 90% conversion for CO oxidation at 620 K in the $SrTi_{0.7}Co_{0.3}O_3$ sample and 100% NO reduction at 920 K for the nanocomposite $CuO/SrTi_{0.7}Co_{0.3}O_3$ sample.[10] Gurav *et al.* studied the $SrTi_{1-x}Ru_xO_3$ system for the dry reforming of methane and achieved approximately 93% CH_4 conversion for 100 h at 1070 K with $SrTi_{0.85}Ru_{0.15}O_3$.[11] López-Suárez *et al.* showed that the $SrTi_{0.89}Cu_{0.11}O_3$ system can be considered as a low-cost alternative material for catalysts that contain noble metals for soot combustion[12] and NOx storage and reduction.[13] They showed that the material achieved 50% soot conversion at 870 K[12] and that the storage of NOx was 41 μmol m^{-2} at 570 K, higher than that on noble metal-containing catalysts used as references by the authors.[13]

Copper-based materials are also active for the water-gas shift (WGS) reaction.[17–21] A previous study in the literature on the WGS reaction based on lanthanum and copper perovskite samples found that the CO conversion was approximately 55% at 560 K for 6 h with $La_{1.85}Ca_{0.15}CuO_4$.[20] The aforementioned results indicate that the $SrTi_{1-x}Cu_xO_3$ system is interesting for future catalysis studies.

Herein, we synthesized $SrTi_{1-x}Cu_xO_3$ (x = 0, 0.03, 0.06, 0.09, 0.12 and 0.15) nanostructured samples using a modified polymeric precursor method, which was previously applied by our group for the synthesis of doped and undoped $SrTiO_3$ compounds.[22] The structural and local atomic properties of the samples were studied in detail using *ex situ* and *in situ* X-ray absorption spectroscopy (XAS), X-ray diffraction (XRD), X-ray photoelectron spectroscopy (XPS) and temperature-programmed reduction (TPR) analyses.

Materials and methods

Materials synthesis

The samples were prepared using the polymeric precursor method and details can be found elsewhere.[22,23] $Sr(NO_3)_2$, $Ti[OCH(CH_3)_2]_4$

[a] *São Carlos Institute of Physics, University of São Paulo, PO Box 369, 13560-970, São Carlos, SP, Brazil. E-mail: valmor@ifsc.usp.br*
[b] *São Carlos Institute of Chemistry, University of São Paulo, 13560-970, São Carlos, SP, Brazil*
[c] *Universite Paris-Est Creteil Val de Marne, ICMPE-CNRS, Thiais, France*

† Electronic supplementary information (ESI) available: X-ray diffraction patterns of samples reduced at 1100 K and XPS spectra in Sr, Ti, O and C regions. See DOI: 10.1039/c5cp05939a

and $Cu(NO_3)_2{\cdot}3H_2O$ were used as precursors. All chemicals were of analytical grade and were used without further purification. Stoichiometric amounts of $Sr(NO_3)_2$ and $Cu(NO_3)_2{\cdot}3H_2O$ were mixed with citric acid in distilled water, and the molar ratio of the cations Sr + Cu to citric acid was 4 : 1. The titanium citrate solution was prepared by dissolving citric acid and titanium isopropoxide in distilled water, and the citric acid to Ti molar ratio was 4 : 1. The resin was prepared by mixing the strontium–copper and titanium solutions, maintaining the molar ratio of Sr : Ti + Cu at 1 : 1. Ethylene glycol was added as a polymerizing agent with an ethylene glycol : citric acid mass ratio of 40 : 60. The obtained resin was dried at 600 K for 8 h to obtain a precursor powder sample. Then, the precursor powder samples were heat-treated under a N_2 flow at 1050 K for 2 h. To remove carbon, the sample was treated under an O_2 flow at 800 K for 2 h, milled and treated again using the same parameters.

Characterization

The crystal structures were analyzed by X-ray powder diffraction (XRD). *Ex situ* diffraction patterns were recorded on a Rigaku Ultima IV diffractometer with Cu Kα radiation (λ = 1.54 Å) at 2θ = 20°–100° with a 0.02° step size and measuring time of 3 s per step. Rietveld refinement procedures were applied for the crystal structure analysis using GSAS software.[24] In the Rietveld refinements, the CIF files (Crystallographic Information File) of $SrTiO_3$ (80873), CuO (16025) and $SrCO_3$ (15195) were used as model crystallographic structures. *In situ* X-ray diffraction patterns were measured by the XPD beamline of the National Laboratory of Synchrotron Light (LNLS, Campinas-Brazil, proposal number 17001) using a Huber diffractometer, Arara furnace and Mythen detector. The parameters were a two-theta range from 35° to 45°, a step of 2.5° and 10 s of acquisition per point, with radiation of λ = 1.5498 Å, selected with a Si(111) monochromator. After performing the measurements under ambient conditions, the samples were heated in a hydrogen-rich atmosphere (5% H_2/He) with a flow rate of 60 mL min^{-1} from 300 to 550 K (reduction temperature) at 10 K min^{-1}. Immediately after the temperature of 550 K was reached, diffraction patterns were periodically recorded *in situ* with the temperature maintained at 550 K.

Field-emission gun scanning microscopy (FEG-SEM) was carried out with a Zeiss Sigma microscope operated at 4 kV. The samples were dispersed in isopropyl alcohol and the suspensions were sonicated and deposited on the substrates. The average particle size was estimated by measuring 500 particles from FEG-SEM images.

Transmission electron microscopy (TEM) was carried out with a Phillips CM200 microscope operated at 200 kV. The samples were dispersed in isopropyl alcohol and the suspensions were sonicated and deposited on Cu grids.

Temperature programmed reduction (TPR) measurements were conducted using a Micromeritics Chemisorb 2750 with 100 mg of sample and a 25 mL min^{-1} flow rate of 5% H_2/Ar gas. The H_2 consumption was measured using a TCD detector.

X-ray photoelectron spectra (XPS) were obtained using a conventional instrument equipped with a high-performance hemispherical analyzer with a 128-channel detector and non-monochromatic Al Kα ($h\nu$ = 1486.6 eV) radiation as the excitation source (K-Alpha Thermo Scientific) at the Brazilian Nanotechnology National Laboratory (LNNano, Campinas-Brazil, proposal number 19123). The operating pressure in the ultrahigh vacuum chamber (UHV) during analysis was 10^{-9} Pa. Energy steps of 200 and 20 eV were used for the survey and single-element spectra, respectively. Peak decomposition was performed using curves with a 70% Gaussian type and a 30% Lorentzian type, as well as a Shirley nonlinear sigmoid-type baseline. The following peaks were used for the quantitative analysis: C 1s, Cu 2p, Ti 2p and Sr 3d. Molar fractions were calculated using peak areas normalized based on the acquisition parameters after a Shirley background subtraction and corrected with experimental sensitivity and transmission factors provided by the manufacturer. The C–(C, H) component of the C 1s peak of adventitious carbon was fixed to 284.5 eV to set the binding energy scale, and the data treatment was performed using CasaXPS software (Casa Software Ltd, UK).

XANES and EXAFS spectra at the Cu and Ti K-edges were obtained in transmission mode by the XAFS2 beamline of the National Laboratory of Synchrotron Light (LNLS, Campinas-Brazil, proposal number 15960), which was operated at 1.36 GeV and 100–160 mA. The powder sample was mixed with boron nitride and the mixture was placed in a cylinder, wherein an adequate pressure was applied to compact the mixture into pellet form, and was then placed in a sample holder with a normal incidence to the X-ray beam. XAS spectra were first obtained under *ex situ* conditions and then *in situ* in a hydrogen-rich atmosphere (5% H_2/He) with a flow rate of 60 mL min^{-1} from 300 K to 500 K at 10 K min^{-1}. Under the reduction conditions, the EXAFS spectra at the Cu K-edge were only collected when we observed that the XANES spectra did not change with time.

For XANES measurements at the Cu K-edge, the spectra were obtained using a step of 3 eV at the pre edge region (8.88–8.96 keV), 0.5 eV step around the edge (8.96–9.05 keV) and 2 eV at the post edge region (9.05–9.15 keV) with 2 s of acquisition per point for all ranges. At the Ti K-edge, the step was 3 eV at the pre edge region (4.90–4.96 keV), 0.3 eV around the edge (4.96–5.05 keV) and 2 eV at the post edge region (5.05–5.15 keV) with 2 s of acquisition per point for all ranges. For comparison among the different samples, all spectra were subjected to background removal and normalized using the first EXAFS oscillation as unity.

Linear combination analysis (LCA) and Principal Component Analysis (PCA) of XANES spectra were performed, including singular value decomposition of the data matrix and target transformation of spectra for the two model compounds.[25,26] These analysis were performed with the MAX-StraightNoChaser XAFS data analysis code.[27]

EXAFS spectra at the Cu K-edge were collected using a 1 eV energy step for the range of 8.96–9.05 keV and 2 eV for the range of 9.05–9.90 keV, with an acquisition time of 2 s per point for all the ranges. A range of k from 1.8 to 12.8 $Å^{-1}$ was selected for calculation of the $k^3\chi(k)$ Fourier transform. To fit the contribution of the first coordination shell around Cu atoms,

the inverse Fourier transform EXAFS spectra were calculated in the R range from 0.92 to 2.07 Å for EXAFS spectra obtained at room temperature and from 1.38 to 2.84 Å for the EXAFS spectra obtained at 550 K in a hydrogen-rich atmosphere (reduced samples). The filtered EXAFS spectra, obtained from the inverse Fourier transform, were processed using the Multiplatform Applications for XAFS code (MAX), with the amplitude and phase shift functions being calculated using the FEFF8.2 *ab initio* code. A CuO sample was used as a model for samples at room temperature, whereas Cu was used for the samples measured at 550 K in a hydrogen-rich atmosphere.[27,28]

Results and discussion

Fig. 1 presents the room temperature XRD patterns and Rietveld refinements of the as-prepared $SrTi_{1-x}Cu_xO_3$ samples. As shown in Fig. 1a, all the samples share the same crystalline phase and were identified as a perovskite-type structure with space group $Pm\bar{3}m$, and the peaks match with that of $SrTiO_3$ cubic symmetry (ICSD No: 80873). As expected, the crystalline phase corresponding to the x = 0.0 (w/o copper) sample was identified as $SrTiO_3$. For the x = 0.03 sample, the major crystalline phase was also $SrTiO_3$ because of the small amount of copper compound added in this sample. Additional minor peaks present in all XRD patterns that do not belong to the $SrTiO_3$ phase were attributed to the formation of adventitious strontium carbonate.[22] The XRD patterns of the samples with x = 0.06 to 0.15 also showed the

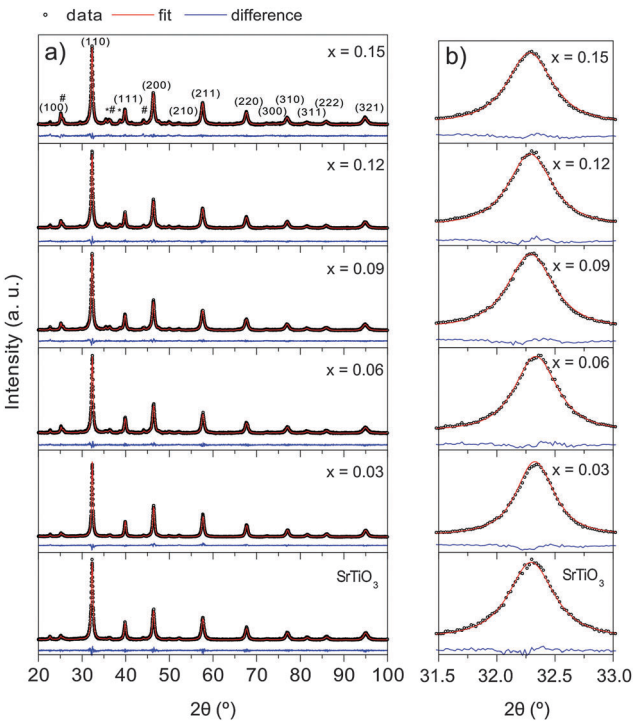

Fig. 1 (a) X-ray diffraction patterns of $SrTi_{1-x}Cu_xO_3$ ($0 < x < 0.15$) samples. Crystallographic indexes correspond to $SrTiO_3$ phase, "*" to CuO, "#" to $SrCO_3$ and "+" to Si. (b) Selection of the range of the main diffraction peak of the $SrTiO_3$ phase.

Table 1 Rietveld refinement results for the lattice parameter and percentage of CuO crystalline phase and error factors weighted profile R-factor (R_{wp}), expected R-factor (R_{exp}) and goodness of fit (χ^2) for $SrTi_{1-x}Cu_xO_3$ samples

x	Lattice parameter (Å)	% of crystalline CuO phase	R_{wp}	R_{exp}	χ^2
0.00	3.91110 ± 0.00010	—	0.1386	0.1290	1.161
0.03	3.91177 ± 0.00008	—	0.0860	0.0732	1.390
0.06	3.91450 ± 0.00010	1.4 ± 0.1	0.1155	0.0695	2.778
0.09	3.91631 ± 0.00009	3.6 ± 0.1	0.0761	0.0629	1.475
0.12	3.91526 ± 0.00008	5.6 ± 0.1	0.0706	0.0625	1.284
0.15	3.91710 ± 0.00010	6.9 ± 0.2	0.0772	0.0564	1.890

$SrTiO_3$ perovskite crystalline phase and two additional minor peaks at 35.6° and 38.7° corresponding to the CuO phase. As x increases from 0.06 to 0.15, an increase in intensity of the CuO peaks is observed, indicating that the segregation of CuO in the samples increased. The crystalline CuO phases in the samples were determined by Rietveld refinement, and the results are shown in Table 1. The sample with x = 0.03 does not show any CuO phase, likely due the limited detection of the XRD technique. Fig. 1b shows the most intense peak in the XRD patterns of $SrTi_{1-x}Cu_xO_3$, which is located at 32.3° and indexed to the (110) plane. A peak shift to lower angles was observed for x = 0.06, 0.09, 0.12 and 0.15. This peak shift suggested the substitution of Ti^{4+} by Cu^{2+} ions because the ionic radius of Cu^{2+} (0.73 Å) is larger than that of Ti^{4+} (0.61 Å), leading to an expansion of the unit cell of the perovskite structure. The lattice parameters of the $SrTi_{1-x}Cu_xO_3$ samples are shown in Table 1. The lattice parameter of the pure $SrTiO_3$ crystal was determined to be 3.91110 Å, which is in good agreement with that reported in the CIF card.[29] The lattice parameter increased with increasing Cu^{2+} ion substitution in the Ti^{4+} site (Table 1). The fit quality was determined by R and χ^2 factors, which are in good agreement with the expected values.[30] For higher values of Cu^{2+} ions ($x > 0.09$), Fig. 1 shows that the peak shift to lower angles was lower than for $x < 0.09$ samples. However, despite the small peak shift to lower angles for the sample with $x > 0.09$, the Rietveld refinement results (Table 1) showed that the lattice parameter of $SrTiO_3$ continued to increase with increasing concentration of substitution Cu^{2+} ion substitution (x = 0.15), except for the lattice parameter of x = 0.012 sample, which is lower than of the $x <$ 0.09 samples.

Different experimental and theoretical studies show that the substitution of Ti^{4+} on the $SrTiO_3$ network by a lower oxidation state metal atom, such as Fe^{3+}, Co^{2+} and Ni^{2+}, promotes the formation of oxygen vacancies. Due to the difference in the oxidation states between titanium (Ti^{4+}) and lower oxidation state atoms, oxygen vacancies are commonly observed in order to maintain the charge balance. Following the previous studies, the doping of Cu^{2+} into Ti^{4+} sites, with oxygen vacancy charge compensation, can be described according to the following equation.[31–34]

$$CuO + Ti_{Ti}^{\times} + O_O^{\times} \rightarrow Cu_{Ti}^{''} + V_O^{\bullet\bullet} + TiO_2 \quad (1)$$

where the process of substitution was represented using the Kroger Vink notation, with $Ti_{Ti}^{\times}$ meaning Ti^{4+} in a Ti^{4+} site, $Cu_{Ti}^{''}$ is Cu^{2+}

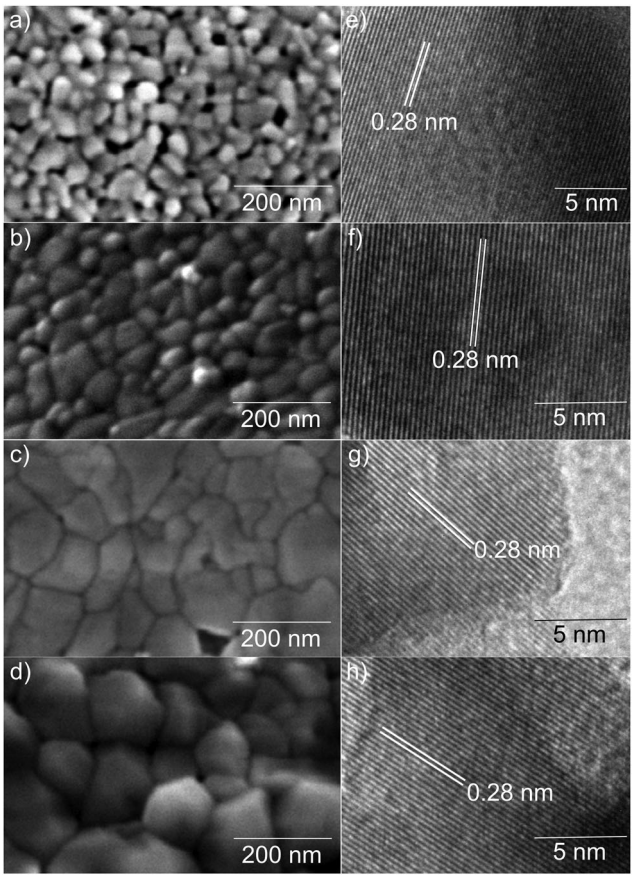

Fig. 2 FEG-SEM images of $SrTi_{1-x}Cu_xO_3$ samples with x = 0.00 (a), 0.03 (b) 0.09 (c) and 0.15 (d) and high resolution TEM images for each sample (e–h) collected at room temperature.

in a Ti site (2 less positive charges), $O_O^{\times}$ is O^{2-} in an O^{2-} site; $V_O^{\bullet\bullet}$ is a O^{2-} vacancy (2 less negative charges).[32]

The morphology and size of the particles were evaluated from FEG-SEM and HRTEM images. Fig. 2 shows FEG-SEM and high resolution TEM images for the $SrTi_{1-x}Cu_xO_3$ samples with x = 0.00, 0.03, 0.09 and 0.15. Fig. 2a shows that the $SrTiO_3$ particles are agglomerated as expected from the polymeric precursors method; however, the boundaries are well defined, since the calcination in an N_2 atmosphere prevented coalescence.[22] The size distribution histogram, presented in Fig. S1 (ESI†), revealed that the mean diameter samples significantly increased with increasing concentration of Cu substitution levels in the lattice of $SrTiO_3$. Fig. 2b shows that the substitution of 3% of titanium atoms for copper atoms modified the size and morphology of the particles, becoming more compact than that of pure $SrTiO_3$ with a mean diameter of 64 ± 13 nm. The size distribution histogram, presented in Fig. S1 (ESI†), revealed that the 9% and 15% NPs presented a mean diameter of 95 ± 27 and 134 ± 31 nm, respectively. A similar behavior was observed by Lee and Huang after increasing the CuO doping in $Ba_{0.4}Sr_{0.6}TiO_3$.[35] The high-resolution images (Fig. 2e–h) show atomic planes separated by 0.28 nm, which is attributed to the space between the (110) planes of the $SrTiO_3$ phase and is in agreement with the X-ray diffraction results.

Fig. 3 presents the TPR profiles of the $SrTi_{1-x}Cu_xO_3$ ($0 < x < 0.15$) samples. The main TPR peak is located at approximately 500 K, and for some samples, the TPR profile presents a shoulder. López-Suárez *et al.* compared the TPR profiles of copper supported on $SrTiO_3$ and copper substituting titanium sites and showed that surface copper is reduced at a lower temperature than copper incorporated into the matrix.[12]

The peak shape observed in our TPR results can be attributed to a convolution of the reduction profiles of incorporated and segregated copper. However, for 15% substitution in the titanium site, no shoulders are observed, indicating the predominance for segregated copper. Reduction peaks are also observed over 900 K, similar to those found by Albaladejo-Fuentes *et al.* for $BaTi_{1-x}Cu_xO_3$, which were attributed to a reduction or desorption of oxygen from the surface and the decomposition of carbonate.[36] A TPR profile of the $SrTi_{0.85}Cu_{0.15}O_3$ sample was collected at 1100 K for 30 min and its X-ray diffraction pattern was collected (see ESI,† Fig. S2). The peak of the $SrCO_3$ phase, which was present prior to the reduction, did not appear in the pattern of the reduced sample, indicating that the TPR reduction over 900 K can be attributed to carbonate decomposition apart from oxygen reduction or desorption.

XPS measurements were performed to monitor the chemical compositions and oxidation states of components present on the surfaces of the as-prepared samples. Fig. 4 and 5 present the spectra for the samples with x = 0.03 to 0.15 in the region of Cu 2p peaks. The satellite peaks indicate the presence of Cu^{2+} in all the samples.[37]

The peaks of the $2p_{1/2}$ and $2p_{3/2}$ orbitals are in displaced positions, compared to those of CuO and are fitted well with two components, suggesting the presence of CuO and copper interacting with the matrix on the surface.[12] With increasing substitution of titanium atoms for copper atoms, the relative intensity of the satellite peaks and the contribution of the components of CuO increase, consistent with the increase in CuO content observed in the X-ray diffraction measurements.

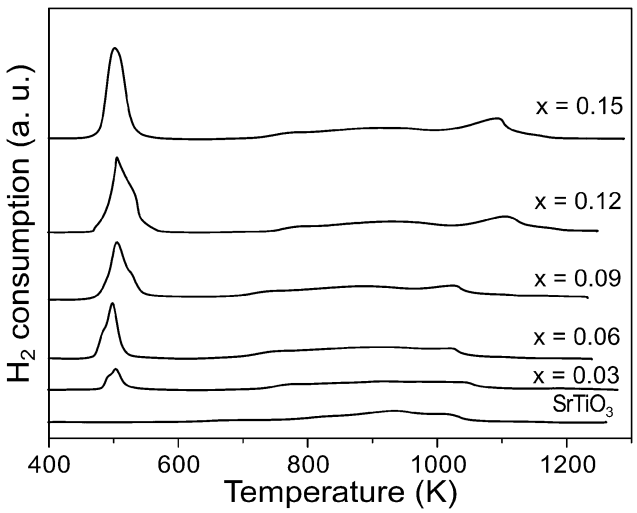

Fig. 3 TPR profiles of $SrTi_{1-x}Cu_xO_3$ samples.

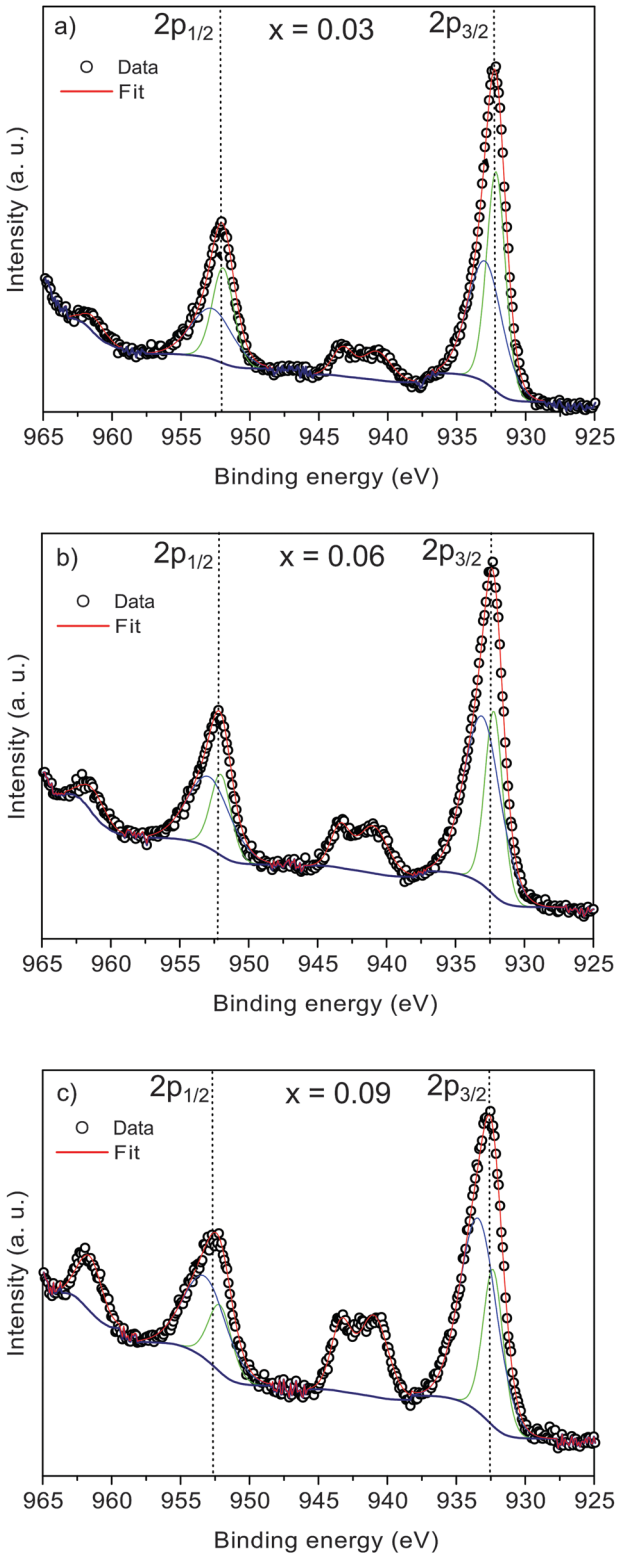

Fig. 4 XPS spectra of the $SrTi_{1-x}Cu_xO_3$ samples with x = 0.03 (a), 0.06 (b) and 0.09 (c) in the region of Cu 2p peaks. XPS spectra collected at room temperature.

The XPS spectra of the Ti 2p, Sr 3d and O 1s are shown in Fig. S3 (see ESI†). The binding energy values for Sr, Ti and O are close to those reported for $SrTiO_3$.[38]

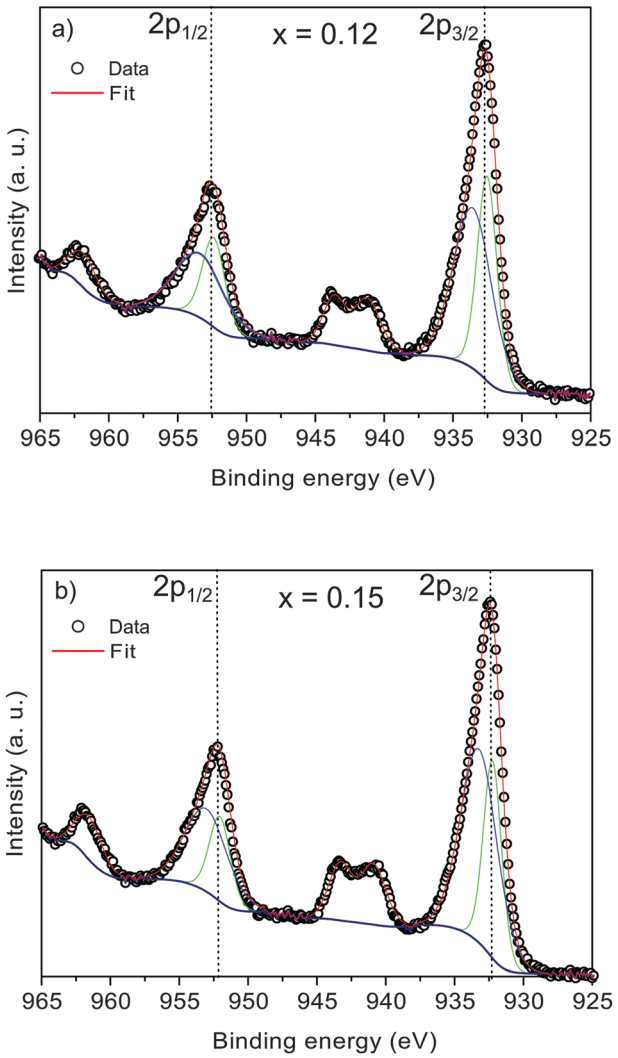

Fig. 5 XPS spectra of $SrTi_{1-x}Cu_xO_3$ samples with x = 0.12 (a) and 0.15 (b) in the region of Cu 2p peaks. XPS spectra collected at room temperature.

Table 2 shows the quantification (% in atoms) of the elements and the corresponding binding energies (BE) of the high-spin orbitals. The amount of Cu on the surface increases as x increases over 0.09, indicating that the copper atoms are mostly segregated in this range of substitution. The high decrease in the quantity of Ti may be attributed to the formation of a strontium carbonate phase.

To confirm that copper, specifically, was reduced during TPR at 550 K, we conducted *in situ* X-ray diffraction experiments under a hydrogen-rich atmosphere. The two-theta scanning range consists of the main peaks of the perovskite phase as well as the main peaks of both the CuO and Cu crystalline phases, enabling us to follow the phase transformation evolution during the reduction process.

Fig. 6 presents the *in situ* XRD patterns of $SrTi_{0.85}Cu_{0.15}O_3$. The CuO phase starts reducing to metallic copper 12 min after the temperature reached 550 K.

In situ and *ex situ* XAS experiments were conducted to investigate the local atomic structure of the Cu-doped $SrTiO_3$

Table 2 Binding energies (BE) and atomic percentages of the elements in $SrTi_{1-x}Cu_xO_3$

	Sr $3d_{5/2}$		Ti $2p_{3/2}$		Cu $2p_{3/2}$	
x	BE (eV)	%	BE (eV)	%	BE (eV)	%
0	132.6	20.63	457.9	12.75	—	—
0.03	132.8	20.59	457.8	6.56	932.2	0.61
0.06	133.1	21.95	457.9	3.80	932.4	0.55
0.09	133.2	22.01	457.9	1.82	932.6	0.40
0.12	133.4	21.84	458.1	4.74	932.7	0.79
0.15	133.0	20.80	457.9	5.56	932.4	1.13

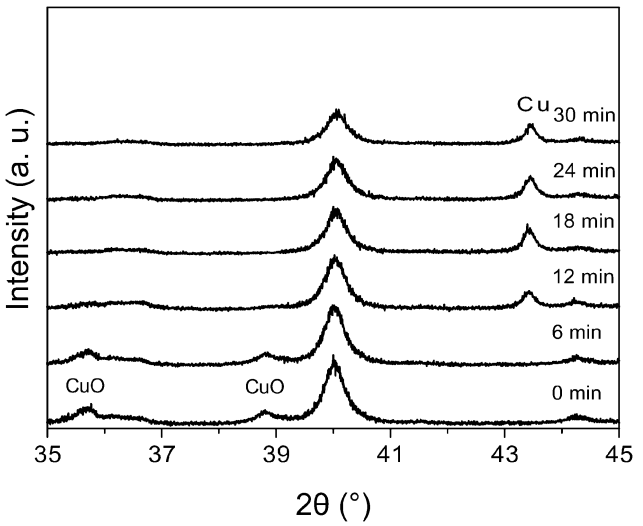

Fig. 6 X-ray diffraction patterns collected at different times for the $SrTi_{0.85}Cu_{0.15}O_3$ sample in a hydrogen-rich atmosphere 30 min. after reaching 550 K.

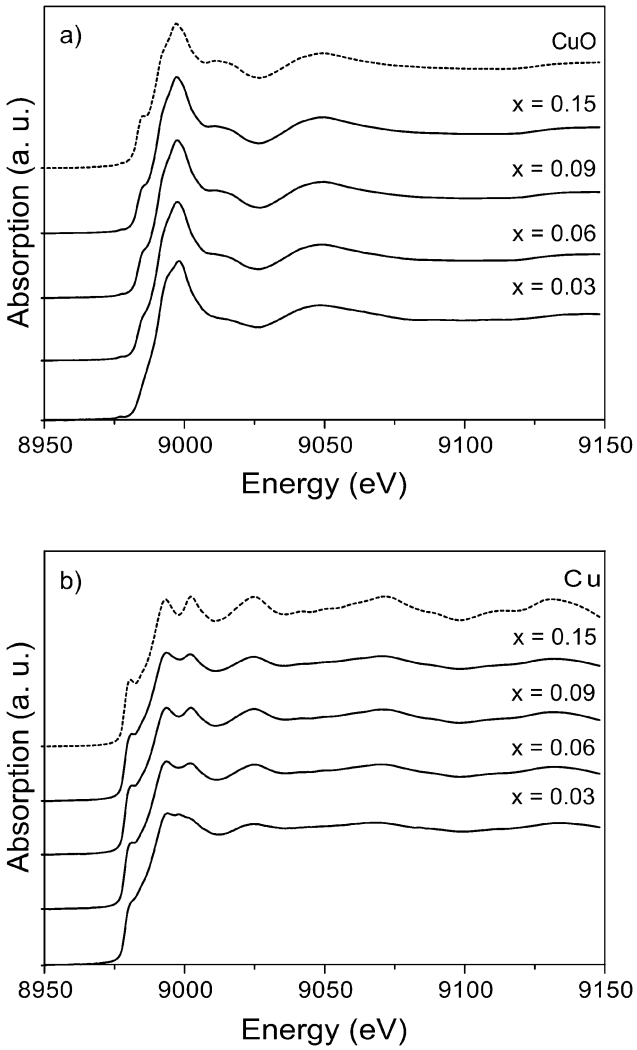

Fig. 7 XANES spectra at the Cu K-edge of $SrTi_{1-x}Cu_xO_3$ (a) at room temperature under ambient atmosphere and (b) a hydrogen-rich atmosphere after reaching 550 K. CuO and Cu standards are shown for comparison.

nanomaterials. Fig. 7 shows the XANES spectra of $SrTi_{1-x}Cu_xO_3$ samples in both ambient (300 K) and hydrogen-rich atmospheres (550 K). The XANES spectrum of the $SrTi_{0.97}Cu_{0.03}O_3$ sample (x = 0.03) is slightly different from that of the CuO phase, indicating that copper has a chemical environment different than in CuO, suggesting in this case, only the occupation of titanium sites by copper atoms. A similar behavior was observed by Beale *et al.* for Ni-doped $SrTiO_3$.[32] For samples with $x > 0.03$, the XANES spectrum becomes more correlated to the CuO standard, in agreement with diffraction results, which shows an increase in CuO formation with the increase in substitution levels of titanium by copper.

For the H_2-reduced samples, the shape of the XANES spectrum of the $SrTi_{0.97}Cu_{0.03}O_3$ sample is not similar to that of the Cu standard foil, which confirms that the reduction process in x = 0.03 is different. This result confirmed that copper atoms only substituted Ti atoms in the lattice. For the samples with high Cu concentrations, the XANES spectra are closer to that of the Cu foil, indicating that segregated copper has a better reducibility than does incorporated copper.

Since the samples were synthesized by insertion of Cu(II) from CuO into the $SrTiO_3$ matrix, we expect the presence of a structure close to CuO in the XANES spectra before reduction. After reduction, we expect the presence of XANES spectra similar to copper metal. The PCA of the data proves definitively that all the XANES spectra can be decomposed on the basis of two components. We tested the two expected standards, Cu metal and CuO, by Target Transformation. They fit reasonably, but not perfectly, showing that the local structure around Cu in the samples is close but not equal to the standards.

The linear least-square fitting results obtained for spectra measured at room temperature under ambient atmosphere (oxidized) and measured in a hydrogen-rich atmosphere after reaching 550 K (reduced) samples are presented on Table S1 (see ESI†). As an example, Fig. S4 (ESI†) on the support information shows the XANES spectra linear least-square fitting for x = 0.03 and x = 0.15 oxidized and reduced samples. The oxidized samples contain only Cu(II) species close to the CuO phase, except for the x = 0.03 sample, in which the fitting quality factor is the worst and is consistent with the assessment that Cu atoms in this sample are preferentially substituting the

Ti site. Moreover, if the Cu metal phase is introduced in the fitting as a second phase, negative coefficients are obtained.

The reduced samples are mainly composed of Cu metal, although a small amount of CuO cannot be totally ruled out for $x \geq 0.06$. For the $x = 0.03$ sample, the compound with the lowest Cu concentration, the quality factor of the linear combination fitting was significantly improved when a larger amount of the CuO phase was considered. We believe that the differences between experimental and linear least-square fitting spectra are more likely due to some disorder in the local structure around Cu atoms. Moreover, we do not observe any edge energy shifts characteristic of a Cu(0) + Cu(II) mixture and as can be seen on Fig. 9, the EXAFS signals of reduced samples are in phase with the EXAFS spectra of Cu metal and the only difference observed is a reduction on the oscillation amplitudes. This disorder effect could be due either to distortions of the local Cu metal structure, or a surface effect if the metallic copper species are organized as very small nanoparticles.

We also obtained EXAFS spectra of the samples to obtain a more quantitative description of the local order around the copper atoms before and after the hydrogen-rich atmosphere treatment. Fig. 8 presents the EXAFS spectra and their respective Fourier transform (FT) of $SrTi_{1-x}Cu_xO_3$ samples at 300 K under ambient conditions. At 300 K, the EXAFS spectra for the $x = 0.03$ sample presents a lower amplitude, indicating a larger degree of disorder or a difference in the local structure around Cu atoms. For $x \geq 0.06$, the EXAFS spectra and their respective FT are similar to the data for the standard CuO phase, indicating that copper is mostly segregated.

Fig. S5 in the ESI,† shows the filtered inverse Fourier transform EXAFS spectra of oxidized samples considering the range between 2.07 and 6.5 Å. The spectra of the $x = 0.06$, $x = 0.09$ and $x = 0.15$ are quite similar of that of the CuO standard spectra. On the other hand, the spectra of the $x = 0.03$ sample present some differences, mainly at higher K values, showing that its local structure is different from the other samples and also of the CuO standard. These results support our supposition that Cu in $x = 0.03$ is substituting Ti atoms at the Ti site, whereas for the other samples, Cu atoms are mainly at the CuO phase.

The EXAFS spectra of the reduced samples and their respective Fourier transform are presented in Fig. 9 along with the data of the standard Cu foil sample for comparison. Although the spectra are in phase with the EXAFS spectra of Cu metal, the intensity of the EXAFS spectra and the Fourier transform of all the reduced samples are considerably lower than for the standard Cu foil. It is important to note that the EXAFS spectra of the samples were collected at 550 K, whereas the spectra of the Cu foil was collected at 300 K.

After reduction, the FT curve of the $x = 0.03$ sample also presents a peak centered on $R = 2.52$ Å, the distance that corresponds to the Cu–Cu interaction. Fig. S6 in the ESI,† shows the filtered inverse Fourier transform EXAFS spectra of reduced samples, corresponding to the first coordination shell around Cu atoms. In this figure, it can be observed that the filtered inverse Fourier transform EXAFS spectra of the samples are similar to that of the Cu metal model, indicating

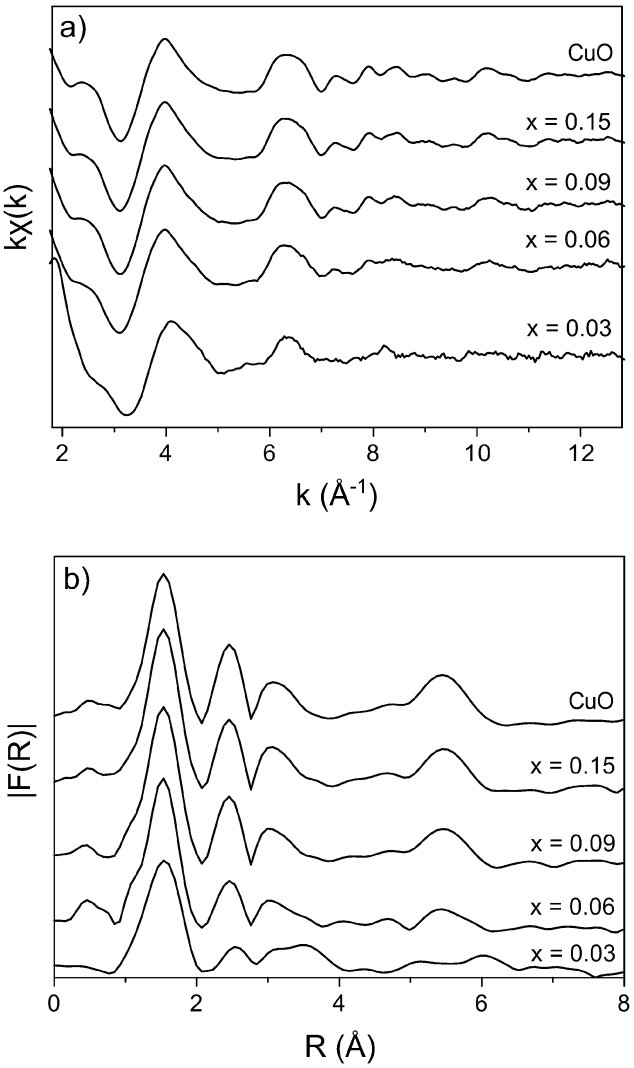

Fig. 8 EXAFS spectra at the Cu K-edge (a) and their respective Fourier transform (b) for $SrTi_{1-x}Cu_xO_3$ samples at room temperature under an ambient atmosphere. The CuO standard is shown for comparison.

only the presence of Cu–Cu interactions, even for the $x = 0.03$ sample.

To confirm the linear combination analysis, and determine if the first neighbors of copper are composed uniquely by oxygen in the oxidized sample and copper in the reduced sample, we performed a non linear fitting of the inverse Fourier Transform EXAFS spectra corresponding to the first coordination shell around the Cu atoms. From these fittings, the coordination number (N), the mean bond-length (R) and the Debye–Waller factor (σ^2) around the Cu atoms before and after hydrogen-rich atmosphere treatment were determined. The results are presented in Table 3. Within the error bar, at oxidizing conditions, the structural parameters of the samples are comparable to that of the CuO phase, confirming the predominance of a local structure around Cu atoms similar to the CuO structure. The fitting results of the $x = 0.03$ sample show that Cu atoms are also coordinated by four oxygen atoms located around 1.95 Å. However, the Debye–Waller factor value is relatively higher,

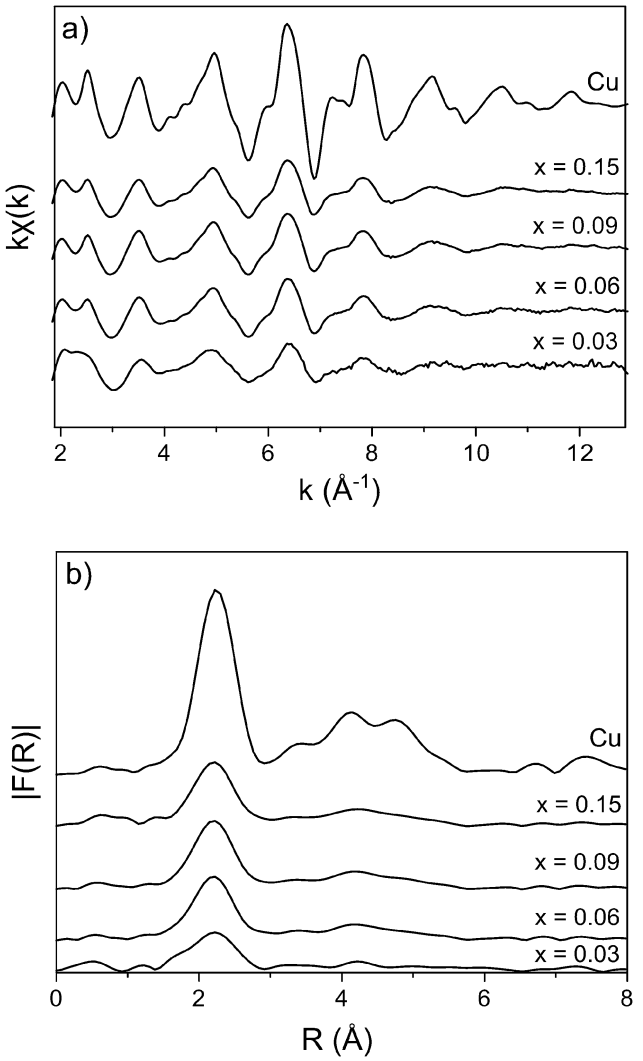

Fig. 9 EXAFS spectra at the Cu K-edge (a) and their respective Fourier transform (b) for $SrTi_{1-x}Cu_xO_3$ samples under a hydrogen-rich conditions at 550 K. The Cu standard data measured at 300 K is shown for comparison.

meaning that Cu atoms in this sample are in a more disordered structure, probably different Cu–O mean bond lengths, when compared to the others samples.

In the case of the reduced samples, the fitting results show a lower coordination number around Cu atoms when compared to the Cu foil and that, for $x \geq 0.06$, the number of Cu–Cu neighbors does not depend on the amount of copper present on the sample. As discussed previously, we attributed this lower Cu–Cu coordination number to a disordered structure of the metallic phase in the reduced samples probably to their nanometric size. Similar results have been observed in different Cu-based catalysts systems.[39,40] Concerning the $x = 0.03$ sample, the lower coordination number and the higher value of the Debye–Waller factor when compared to the others samples support our previous results that in this sample, Cu is preferentially located at the Ti site of the perovskite lattice.

To confirm that Cu atoms are only coordinated by Cu atoms in the reduced samples, we investigated whether any oxygen atoms contributed to the signal of the main peak in the Fourier transform of reduced samples. For this purpose, we used a two-shell model for the simulation, consisting of a first coordination shell of Cu–O and a second shell of Cu–Cu. The simulation results (not shown) provided coordination numbers near zero for Cu–O with a high error bar. Based on these results, we assume that the first coordination shell of all reduced samples consisted only of Cu–Cu interactions.

Table 3 EXAFS fitting results for coordination number (N), Debye–Waller factor (σ^2) and bond length (R) and the quality factor (QF) of $SrTi_{1-x}Cu_xO_3$ samples measured at 300 K and 550 K in ambient and hydrogen-rich atmospheres

	N	σ^2 (Å^2)	R (Å)	QF
Ambient atmosphere-measurements at 300 K				
CuO	4.1 ± 0.4	0.005 ± 0.001	1.948 ± 0.007	1.01
$SrTi_{0.97}Cu_{0.03}O_3$	4.6 ± 0.4	0.011 ± 0.002	1.95 ± 0.01	1.90
$SrTi_{0.94}Cu_{0.06}O_3$	4.3 ± 0.5	0.005 ± 0.001	1.945 ± 0.007	2.16
$SrTi_{0.91}Cu_{0.09}O_3$	4.5 ± 0.4	0.005 ± 0.001	1.946 ± 0.008	1.64
$SrTi_{0.85}Cu_{0.15}O_3$	4.4 ± 0.3	0.0052 ± 0.0005	1.946 ± 0.009	1.45
Hydrogen-rich atmosphere-measurements at 550 K				
Cu foil[a]	12.0 ± 0.6	0.0086 ± 0.0004	2.534 ± 0.004	1.59
$SrTi_{0.97}Cu_{0.03}O_3$	5.8 ± 0.4	0.015 ± 0.008	2.52 ± 0.01	2.06
$SrTi_{0.94}Cu_{0.06}O_3$	7.4 ± 0.4	0.0138 ± 0.0004	2.52 ± 0.01	0.73
$SrTi_{0.91}Cu_{0.09}O_3$	8.0 ± 0.8	0.01 ± 0.04	2.52 ± 0.09	0.57
$SrTi_{0.85}Cu_{0.15}O_3$	7.3 ± 0.9	0.014 ± 0.001	2.52 ± 0.01	0.65

[a] Cu foil EXAFS spectrum was obtained at 300 K.

To confirm that only copper atoms are reduced during the hydrogen-rich atmosphere treatment, *in situ* XANES spectra were also obtained at the Ti K-edge before (300 K) and after reduction (550 K). The main absorption in the Ti XANES spectra presented in Fig. 10 is related to the dipole-allowed excitation of 1s electrons to p orbitals.[41] There are also four characteristic pre-edge peaks at the pre-edge region. The first is associated to the 1s → 3d (t_{2g}) transition, the second is due to the 1s → 4p transition, and the third and the fourth are overlapped and are assigned to a dipole transition of 1s electrons to the t_{2g} and e_g orbitals of the neighboring TiO_6 octahedra.[41] For comparison, we also present the XANES spectra of $SrTiO_3$ collected at 300 K. As can be observed in Fig. 10a and b, if copper atoms substituted titanium atoms, no significant changes were observed in the XANES spectra under ambient and hydrogen-rich atmospheres. Thus, we can conclude that only copper atoms were reduced, whereas the titanium oxidation state remained stable. This result is in agreement with the XRD data, indicating that the long-range order of the perovskite phase remains stable under reducing conditions.

Conclusions

In this study, we used the polymeric precursor method to obtain $SrTiO_3$ and Cu-doped $SrTiO_3$ nanoparticles. The segregation of copper was observed for the $SrTi_{1-x}Cu_xO_3$ system for $x \geq 0.06$, which can be explained by the larger ionic radius of the dopant. The shape of the TPR profiles indicated a difference in the reducibility of incorporated and segregated copper. According to

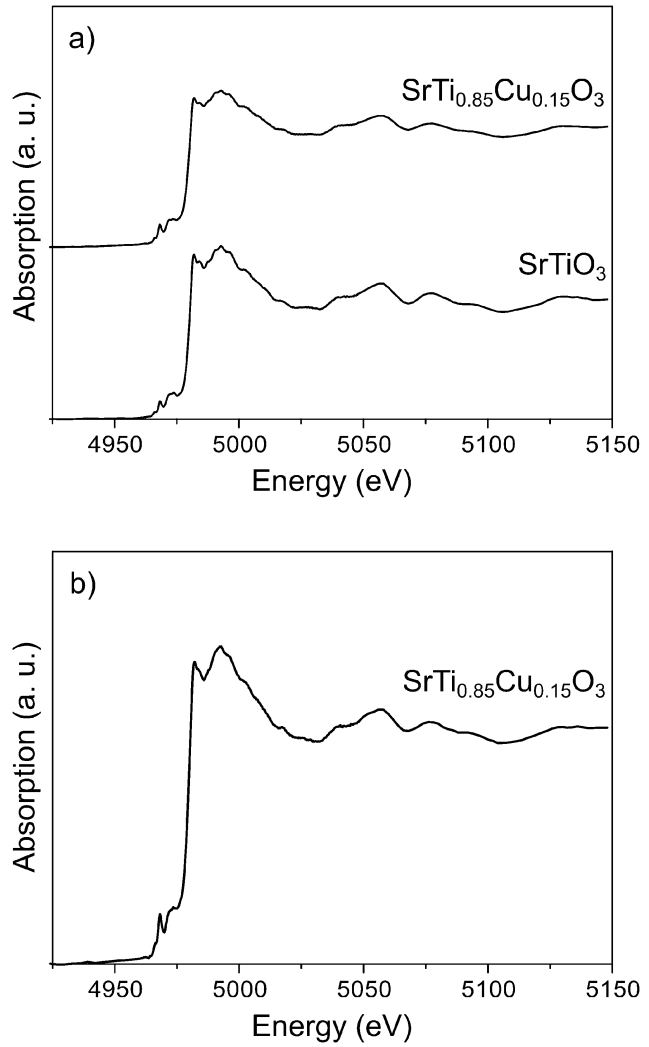

Fig. 10 XANES spectra at the Ti K-edge (a) at room temperature under an ambient atmosphere and (b) reducing conditions.

the *in situ* X-ray diffraction and absorption experiments, this reduction is specific to copper. Because copper in the metallic state is generally active for different catalytic reactions, our results concerning the reduction of copper in $SrTi_{1-x}Cu_xO_3$ samples are a basis for studies of these materials as new catalysts, particularly for the water-gas shift reaction.

Acknowledgements

The authors are grateful for the financial support provided by the São Paulo Research Foundation-FAPESP (grant 2013/09573-3) and the National Council for Scientific and Technological Development-CNPq (grants 304498/2013-0 and 140631/2013-5). Our thanks are also extended to the Brazilian Synchrotron Light Laboratory (LNLS) for the use of its XAFS2 and XPD beam line experimental facilities (proposal numbers 15960 and 17001). We also wish to thank the Brazilian Nanotechnology National Laboratory (LNNano) for the use of the XPS equipment (proposal 19123). The authors are also grateful to Alessandra F. Lucredio for TPR measurements and Marcelo O. Orlandi for the use of the transmission electron microscope.

References

1 V. R. Mastelaro, S. C. Zílio, L. F. da Silva, P. I. Pelissari, M. I. B. Bernardi, J. Guerin and K. Aguir, *Sens. Actuators, B*, 2013, **181**, 919–924.
2 C. L. Chow, W. C. Ang, M. S. Tse and O. K. Tan, *Thin Solid Films*, 2013, **542**, 393–398.
3 R. Moos, N. Izu, F. Rettig, S. Reiss, W. Shin and I. Matsubara, *Sensors*, 2011, **11**, 3439–3465.
4 M. C. Verbraeken, T. Ramos, K. Agersted, Q. Ma, C. D. Savaniu, B. R. Sudireddy, J. T. S. Irvine, P. Holtappels and F. Tietz, *RSC Adv.*, 2015, **5**, 1168–1180.
5 E. Korkmaz, N. Kalaycioglu and V. Kafadar, *Bull. Mater. Sci.*, 2013, **36**, 1079–1086.
6 B. Marí, K. C. Singh, P. Cembrero-Coca, I. Singh, D. Singh and S. Chand, *Displays*, 2013, **34**, 346–351.
7 L. F. da Silva, W. Avansi, M. L. Moreira, A. Mesquita, L. J. Q. Maia, J. Andrés, E. Longo and V. R. Mastelaro, *J. Nanomater.*, 2012, **890397**, 1–6.
8 H. Wang, J. Lu, C. L. Marshall, J. W. Elam, J. T. Miller, H. Liu, J. A. Enterkin, R. M. Kennedy, P. C. Stair, K. R. Poeppelmeier and L. D. Marks, *Catal. Today*, 2014, **237**, 71–79.
9 J. A. Enterkin, W. Setthapun, J. W. Elam, S. T. Christensen, F. A. Rabuffetti, L. D. Marks, P. C. Stair, K. R. Poeppelmeier and C. L. Marshall, *ACS Catal.*, 2011, **1**, 629–635.
10 A. Glisenti, M. M. Natile, S. Carlotto and A. Vittadini, *Catal. Lett.*, 2014, **144**, 1466–1471.
11 H. R. Gurav, R. Bobade, V. L. Das and S. Chilukuri, *Indian J. Chem.*, 2012, **51A**, 1339–1347.
12 F. E. López-Suárez, S. Parres-Esclapez, A. Bueno-López, M. J. Illán-Gómez, B. Ura and J. Trawczynski, *Appl. Catal., B*, 2009, **93**, 82–89.
13 F. E. López-Suárez, M. J. Illán-Gómez, A. Bueno-López and J. A. Anderson, *Appl. Catal., B*, 2011, **104**, 261–267.
14 S. Kawasaki, R. Takahashi, K. Akagi, J. Yoshinobu, F. Komori, K. Horiba, H. Kumigashira, K. Iwashina, A. Kudo and M. Lippmaa, *J. Phys. Chem. C*, 2014, **118**, 20222–20228.
15 L. F. da Silva, W. Avansi, J. Andres, C. Ribeiro, M. L. Moreira, E. Longo and V. R. Mastelaro, *Phys. Chem. Chem. Phys.*, 2013, **15**, 12386–12393.
16 T. D. Thanh, L. M. Oanh, N. Van Minh, J. S. Lee and S. C. Yu, *IEEE Trans. Magn.*, 2014, **50**, 2502704.
17 T. L. LeValley, A. R. Richard and M. Fan, *Int. J. Hydrogen Energy*, 2014, **39**, 16983–17000.
18 C. G. Maciel, T. de F. Silva, E. M. Assaf and J. M. Assaf, *Appl. Energy*, 2013, **112**, 52–59.
19 X. Lin, C. Chen, J. Ma, X. Fang, Y. Zhan and Q. Zheng, *Int. J. Hydrogen Energy*, 2013, **38**, 11847–11852.
20 S. S. Maluf, P. A. P. Nascente, C. R. M. Afonso and E. M. Assaf, *Appl. Catal., A*, 2012, **413–414**, 85–93.

21 C. Ratnasamy and J. P. Wagner, *Catal. Rev.*, 2009, **51**, 325–440.
22 L. F. da Silva, L. J. Q. Maia, M. I. B. Bernardi, J. A. Andrés and V. R. Mastelaro, *Mater. Chem. Phys.*, 2011, **125**, 168–173.
23 L. F. da Silva, M. I. B. Bernardi, L. J. Q. Maia, G. J. M. Frigo and V. R. Mastelaro, *J. Therm. Anal. Calorim.*, 2009, **97**, 173–177.
24 A. C. Larson and R. von Dreele, *General Structure Analysis System (GSAS)*, 1994.
25 S. R. Wasserman, *J. Phys. IV*, 1997, **7**, C2-203–C2-205.
26 S. R. Wasserman, P. G. Allen, D. K. Shuh, J. J. Bucher and N. M. Edelstein, *J. Synchrotron Radiat.*, 1999, **6**, 284–286.
27 A. Michalowicz, J. Moscovici, D. Muller-Bouvet and K. Provost, *J. Phys.: Conf. Ser.*, 2013, **430**, 12016.
28 A. L. Ankudinov, B. Ravel, J. J. Rehr and S. D. Conradson, *Phys. Rev. B: Condens. Matter Mater. Phys.*, 1998, **58**, 7565–7576.
29 Y. A. Abramov, V. G. Tsirelson, V. E. Zavodnik, S. A. Ivanov and I. D. Brown, *Acta Crystallogr., Sect. B: Struct. Sci.*, 1995, **51**, 942–951.
30 B. H. Toby, *Powder Diffr.*, 2006, **21**, 67–70.
31 S. Carlotto, M. M. Natile, A. Glisenti and A. Vittadini, *Chem. Phys. Lett.*, 2013, **588**, 102–108.
32 A. M. Beale, M. Paul, G. Sankar, R. J. Oldman, C. R. A. Catlow, S. French and M. Fowles, *J. Mater. Chem.*, 2009, **19**, 4391–4400.
33 S. Fuentes, P. Muñoz, N. Barraza, E. Chávez-Ángel and C. M. Sotomayor Torres, *J. Sol-Gel Sci. Technol.*, 2015, **75**, 593–601.
34 V. V Laguta, O. I. Scherbina, E. P. Garmash, V. N. Pavlikov, M. V Karpec, M. D. Glinchuk and G. S. Svechnikov, *J. Mater. Sci.*, 2013, **48**, 4016–4022.
35 Y.-C. Lee and Y.-L. Huang, *J. Am. Ceram. Soc.*, 2009, **92**, 2661–2667.
36 V. Albaladejo-Fuentes, F. E. López-Suárez, M. S. Sánchez-Adsuar and M. J. Illán-Gómez, *Appl. Catal., A*, 2014, **488**, 189–199.
37 G. Schön, *Surf. Sci.*, 1973, **35**, 96–108.
38 R. P. Vasquez, *J. Electron Spectrosc. Relat. Phenom.*, 1991, **56**, 217–240.
39 S. D. Lin, T. C. Hsiao and L.-C. Chen, *Appl. Catal., A*, 2009, **360**, 226–231.
40 C. Angelici, F. Meirer, A. M. J. van der Eerden, H. L. Schaink, A. Goryachev, J. P. Hofmann, E. J. M. Hensen, B. M. Weckhuysen and P. C. A. Bruijnincx, *ACS Catal.*, 2015, **5**, 6005–6015.
41 M. Vračar, A. Kuzmin, R. Merkle, J. Purans, E. A. Kotomin, J. Maier and O. Mathon, *Phys. Rev. B: Condens. Matter Mater. Phys.*, 2007, **76**, 174107.